Accepted version for publication. Uploaded for the purposes of the VQR [2020-2024].
https://doi.org/10.1002/adfm.202101510
Volume 31, Issue 28, July 9, 2021, Article number 2101510
id scopus: 2-s2.0-85105169478
WOS:000645561700001

WILEY-VCH

Breaking polymer chains with self-propelled light-controlled navigable hematite microrobots

*Mario Urso, Martina Ussia, and Martin Pumera**

Dr. M. Urso, Dr. M. Ussia, Prof. M. Pumera

Future Energy and Innovation Laboratory

Central European Institute of Technology

Brno University of Technology

Purkyňova 656/123, 612 00 Brno, Czech Republic

E-mail: Martin.Pumera@ceitec.vutbr.cz

Keywords: micromotors, iron oxides, photocatalysis, water purification, polymers, plastics, pollutants

The increasing use of polymers has led to an uncontrollable accumulation of polymer waste in the environment, evidencing the urgent need for effective and definitive strategies to degrade them. Here, self-propelled light-powered magnetic field-navigable hematite/metal Janus microrobots that can actively move, capture and degrade polymers are presented. Janus microrobots are fabricated by asymmetrically depositing different metals on hematite microspheres prepared by low-cost and large-scale chemical synthesis. All microrobots exhibit fuel-free motion capability, with light-controlled on/off switching of motion and magnetic field-controlled directionality. Higher speeds are observed for bimetallic coatings with respect to single metals. This is due to their larger mixed potential difference with hematite as indicated by Tafel measurements. As a model for polymers, the total degradation of high molecular weight polyethylene glycol (PEG) is demonstrated by Matrix-Assisted

Laser Desorption/Ionization Mass Spectrometry (MALDI-MS). This result is attributed to the active motion of microrobots, enhanced electrostatic capture of polymer chains, improved charge separation at the hematite/metal interface, and catalyzed photo-Fenton reaction. This work opens the route towards the degradation of polymers and plastics in water using light.

1. Introduction

Plastics are synthetic polymers made by linking together hundreds to thousands of organic subunits (monomers) via strong covalent bonds.[1] Thanks to their excellent chemical and mechanical stability, low weight and cost, plastics are the most used materials in everyday life, including packaging, constructions and transports.[2] Plastics global manufacturing has increased exponentially since 1950s, overwhelming the world's ability to deal with them. Conventional methods to remove plastic wastes like incineration are inadequate due to environmental constraints.[3] As a consequence, plastics continue to accumulate in the environment. Specifically, the pollution of marine environment with plastics, also referred to as "white pollution", has become one of the most pressing environmental issue.[4] Indeed, plastics do not degrade, but slowly fragment into microplastics, particles smaller than 5 mm, and then into nanoplastics.[5] Such small particles can absorb persistent organic pollutants (POPs) in water, increasing their toxicity.[6] Moreover, they are indigested by organisms that are at the basis of the food chain, causing serious risks for the health of living beings.[7,8] At the current growth rates, 12,000 Mt of plastics waste is expected to be in the environment by 2050, highlighting the necessity for effective strategies to definitely degrade plastics in water.[9]

Photocatalysis represents a promising approach for the degradation of polymeric materials in water, as it simply requires a light source and a catalyst.[10] Among the most used catalysts for the degradation of pollutants in water there are photocatalytic semiconductors

like TiO_2 and ZnO.[11] When the photocatalytic semiconductor is irradiated by photons with energy equal to or higher than its band-gap energy, the photogenerated electron-hole pairs react with water, inducing the formation of reactive oxygen species (ROS) as OH· radicals. These, in turns, lead to a series of oxidation processes that degrade pollutants into CO_2 and H_2O. The achievement of a close contact between the catalyst and the pollutant is crucial for the effectiveness of this method.[12] However, conventional photocatalytic approaches are limited by diffusion, requiring an external agitation to accelerate the degradation process.[13]

Self-propelled micro/nanorobots have demonstrated to overcome these issues, enhancing the interactions with the pollutant.[13-19] Micro/nanorobots are micro/nanomaterials that can navigate in fluids, exploiting the synergy between the enhanced physicochemical properties of materials at the micro/nanoscale and improved diffusion due to the active motion.[20] They are based on asymmetric structures whose autonomous movement can be triggered by an external energy source (light, magnetic fields, ultrasounds) or propelled by a fuel (H_2O_2, enzymes) extracted from their surroundings. The micro/nanorobot asymmetry (e.g. in morphology/shape) is required to obtain an asymmetric generation of products that make it move.[21] Light-driven micro/nanorobots are receiving great attentions, since light is a renewable, powerful and abundant energy source that they can use to move and at the same time induce the degradation of pollutants in water.[22] The most common one is the Janus ("two-faced") microrobot consisting of a photocatalytic semiconducting particle (TiO_2, ZnO, Cu_2O, BiOI) asymmetrically covered with a metal (Pt, Au).[23-26] The motion mechanism and speed of Janus micro/nanorobots are strongly correlated to the design of the semiconductor/metal interface.[27,28] Light-driven TiO_2/Ni/Au Janus microrobots showed the ability to collect and remove microplastics from water.[29] Still, the photocatalytic degradation of polymeric materials in water using microrobots has never been demonstrated.

Hematite (α-Fe_2O_3) is an abundant, low-cost and eco-friendly *n*-type semiconductor with a narrow bandgap of 2.2 eV.[30,31] It also catalyzes Fenton and photo-Fenton reactions

with UV-light irradiation and H_2O_2, producing more ROS to attack pollutants in water.[32] These characteristics make it an appealing material for the fabrication of visible light-powered micro/nanorobots for water remediation. However, hematite photocatalytic applications are limited by its high electron-hole recombination rate and low electron mobility.[30,31] Self-propulsion in hematite-based microrobots has been observed only by the decomposition of H_2O_2, eventually activated by light and at basic pH, displaying self-organization and rheotactic behaviors.[33-37] Furthermore, hematite magnetic field navigability due to its weakly ferromagnetic nature at room temperature has been employed for cargo transport, cell manipulation and patterning.[34,37] Hematite/metal Janus microrobots for the photodegradation of pollutants in water have not been reported yet. Such microrobots hold considerable promise, as an appropriate metal loading could improve the charge separation in hematite, leading to a light-powered and magnetic field-controlled microrobot whose autonomous movement can boost its photodegradation ability.

In this paper, we demonstrate the degradation of polymer chains in water by self-propelled light-powered magnetic field-navigable hematite/metal Janus microrobots (**Scheme 1**). Hematite microspheres were synthesized by a low-cost and large-scale hydrothermal reaction, and asymmetrically covered with different metals to fabricate novel Janus microrobots. All microrobots showed fuel-free self-propulsion under UV-light irradiation, with programmable control over on/off switching and direction of the motion. Differences in microrobots speeds at different fuel concentrations and metal coatings were also evaluated and explained through electrochemical measurements. The photodegradation ability of microrobots towards polymeric materials has been proved using high molecular weight (*Mw* 4000) polyethylene glycol (PEG), a water soluble polymer widely used in cosmetics.[38] PEG has been selected as a model for polymers due to its simple molecular structure, which makes it the ideal sample to evaluate microrobots degradation ability by Matrix-Assisted Laser Desorption/Ionization Mass Spectrometry (MALDI-MS). Microrobots active motion,

electrostatic capture ability, superior charge separation at the hematite/metal interface and catalyzed photo-Fenton reaction led to the effective photodegradation of PEG chains. This work presents an environmental-friendly strategy for the removal of polymeric and plastic materials using abundant and renewable sources like water and light.

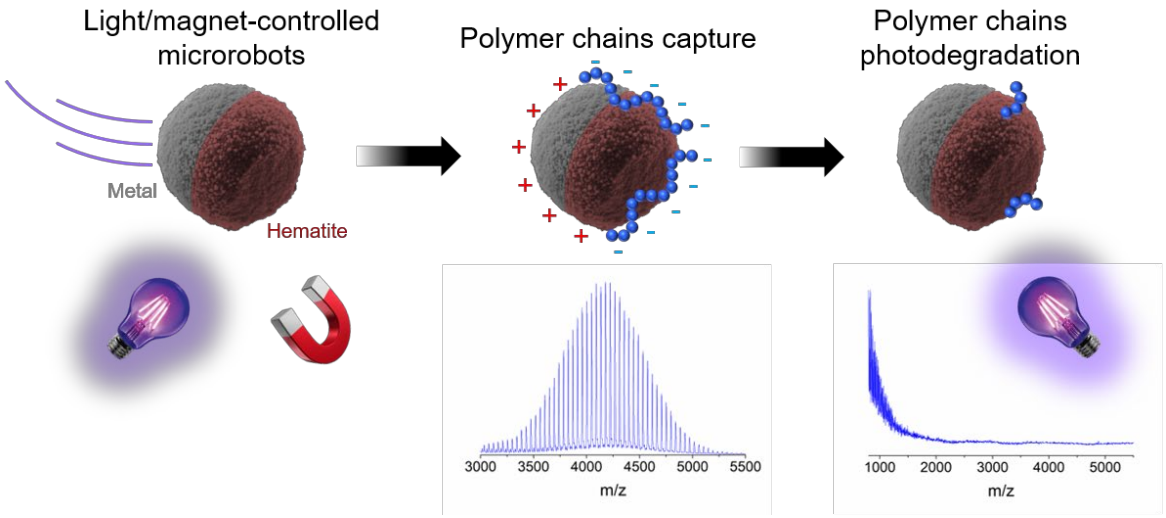

Scheme 1. Self-propelled light-powered magnetic field-navigable hematite/metal Janus microrobots with the ability to capture and photodegrade polymeric materials in water.

2. Results and Discussion

2.1. Fabrication of Hematite/Metal Janus Microrobots

Figure 1 depicts the synthesis procedure and characterization of hematite microspheres. An iron oxide-based particulate was synthesized by a simple hydrothermal reaction, as illustrated in Figure 1(a). The morphology and elemental composition of the obtained sample was characterized by scanning electron microscopy (SEM) and energy dispersive X-ray spectroscopy (EDX). SEM images at different magnification in Figure 1(b-c) demonstrate the formation of spherical microparticles with diameters ranging from 3 to 4 μm. The corresponding EDX images showing the elemental distribution of Fe and O are reported in Figure S1. The high resolution SEM image in Figure 1(d) reveals that they are composed by

50-100 nm large nanoparticles. As a result, such microparticles possess a highly rough surface which is promising for applications. X-ray diffraction (XRD) was carried out to assess microspheres crystalline structure. The XRD pattern reported in Figure 1(d) indicates the presence of pure α-Fe_2O_3 (PDF card # 00-001-1053), occurring in nature as the mineral hematite. Hematite has a rhombohedral crystal structure, where Fe^{3+} cations distribute amongst two thirds of the octahedral interstitial sites between hexagonal close packed O^{2-} planes.[39] The chemical composition of hematite microspheres was characterized by X-ray photoelectron spectroscopy (XPS). Figure 1(e-f) show the high-resolution XPS spectra of Fe 2p and O 1s, respectively. In the Fe 2p spectrum, the two peaks at binding energies 711.0 and 724.4 eV are signals from Fe $2p_{3/2}$ and Fe $2p_{1/2}$, respectively. The corresponding satellite peaks at 718.8 and 732.8 eV binding energies are also observed. These features are attributed to Fe^{3+} cations at octahedral sites in hematite.[40] Both Fe $2p_{3/2}$ and Fe $2p_{1/2}$ peaks were fitted using no less than three components, which reflect the different chemical environments of surface cations. The O 1s core level spectrum shows two components, ascribed to Fe–O within Fe_2O_3 at 529.9 eV binding energy, and OH groups bonded to FeO within FeO(OH) at 531.1 eV.

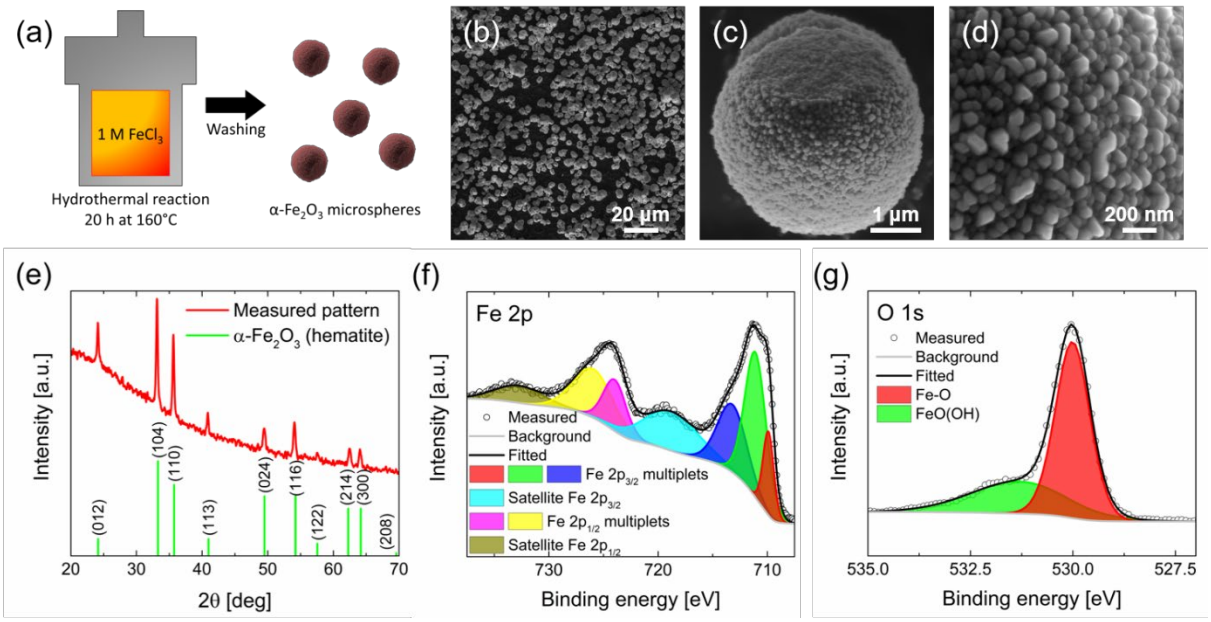

Figure 1. Synthesis and characterization of hematite microspheres. (a) Schematic illustration of the synthesis. (b-d) SEM images at different magnifications. (e) XRD pattern. (f) Fe 2p XPS spectrum. (g) O 1s XPS spectrum.

To observe self-propulsion with spherical hematite microparticles it is necessary to break the symmetry of the system. Hematite/metal Janus microrobots were fabricated by asymmetrically coating hematite microspheres surface with different metals by a physical vapor deposition (PVD) method. As hematite/metal Janus microrobots have never been reported, the scope of this study is also to identify the optimal metal coating leading to higher speed and better photocatalytic activity. Among metals, Au and Pt were selected due to their frequent use for the fabrication of semiconductor/metal Janus micro/nanomotors.[22-28] As it has been recently demonstrated that the bimetallic coating can synergistically enhance photocatalytic microrobots speed, the deposition of Au-Pd and Pt-Pd (80-20 wt%) was also performed.[41] **Figure 2** shows the EDX elemental mapping of the resulting hematite/metal Janus microrobots, proving the presence of Au, Pt and Pd in the four samples and the achievement of the characteristic “two-faced” morphology.

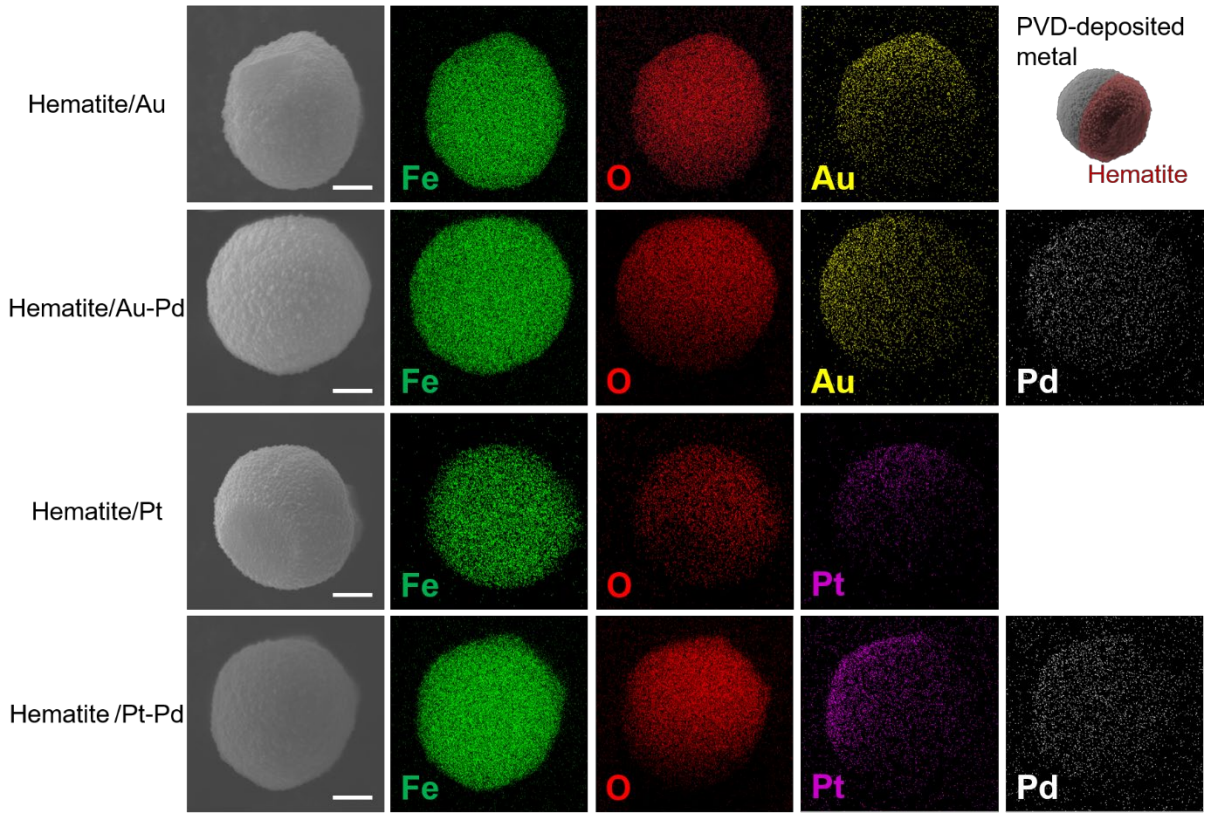

Figure 2. EDX elemental mapping images of hematite/metal Janus microrobots (scale bars are 1 μm).

2.2. Motion Behavior of Hematite/Metal Janus Microrobots

The general motion mechanism for light-powered hematite/metal Janus microrobots is schematically illustrated in **Figure 3**. Photons having energy equal to or higher than hematite bandgap (E_g = 2.2 eV) are absorbed, promoting electrons to the conduction band and leaving holes in the valence band

$$\alpha\text{-}Fe_2O_3 + h\nu \rightarrow e^- + h^+. \quad (1)$$

Bare hematite is characterized by a low electron mobility and high electron-hole recombination rate.[29,30] However, semiconductor/metal junctions have demonstrated to improve charge separation by favoring the transfer of electrons from the semiconductor to the metal.[22-28] Electrons transferred to the metal and holes left in hematite decompose pure water and H_2O_2

fuel (if present) in oxygen and protons. In particular, oxidation of water and H_2O_2 occurs at the hematite side, as follows[42]

$$2H_2O + 4h^+ \rightarrow 4H^+ + O_2 \quad (2)$$

$$H_2O_2 + 2h^+ \rightarrow 2H^+ + O_2. \quad (3)$$

Contemporarily, reduction of protons and H_2O_2 occurs at the metal side, as follows

$$4H^+ + 4e^- \rightarrow 2H_2 \quad (4)$$

$$H_2O_2 + 2e^- + 2H^+ \rightarrow 2H_2O. \quad (5)$$

Protons consumption at the metal side generates a concentration gradient, inducing the migration of protons from hematite to metal. This in turns produces a self-electro-osmotic flow for the propulsion of the Janus microrobot. The proton concentration gradient also creates an electric dipole, and thus a local electric field leading to a self-electrophoretic motion of the Janus microrobot with the hematite side forward, as shown in Figure 3.

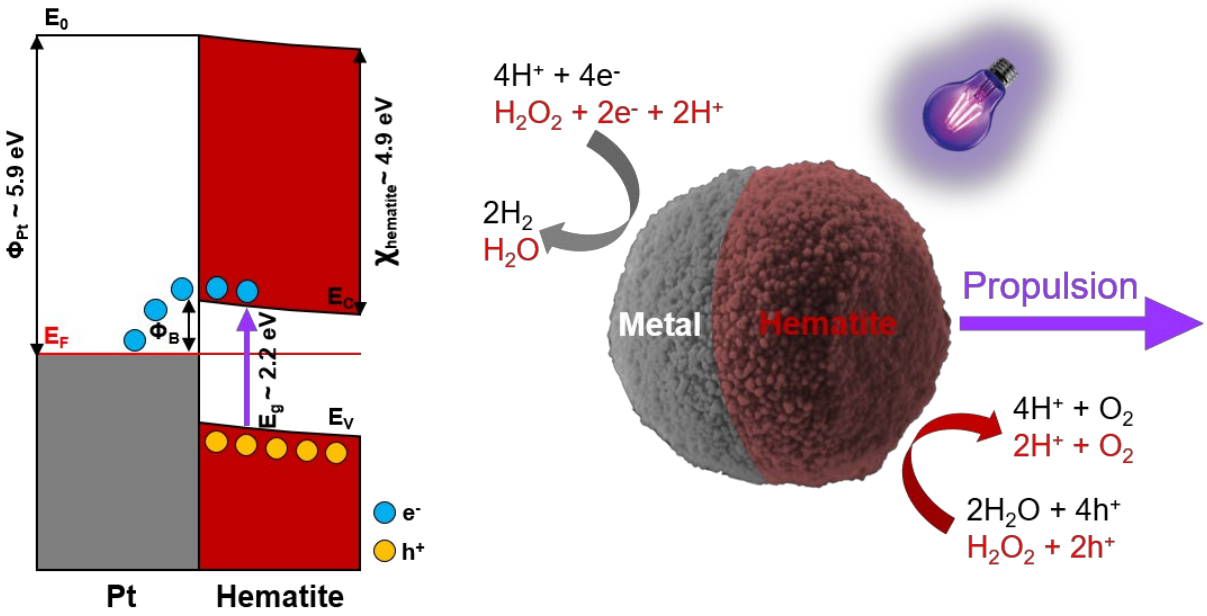

Figure 3. Electron transfer at the hematite/Pt interface and light-powered propulsion mechanism of hematite/metal Janus microrobots. E_F is the Fermi level, E_0 is the vacuum level, E_C and E_V are hematite conduction and valence band levels, E_g is hematite optical bandgap, Φ_{Pt} is Pt work function, $\chi_{hematite}$ is hematite electron affinity, Φ_B is the Schottky barrier.

Motion experiments were first performed in pure water under UV-light irradiation to test the propulsion efficiency of hematite/metal Janus microrobots in fuel-free conditions. It was noticed that bare hematite microspheres showed only Brownian motion with and without light irradiation (Supplementary Movie 1), as expected for a symmetrical particle suffering from high electron-hole recombination rate. All hematite/metal Janus microrobots demonstrated Brownian behavior in dark and motion with linear trajectories under light irradiation (Supplementary Movie 2). To explain the linearity of the observed trajectories, the Brownian rotational time τ_R [s] of our microrobots was calculated using the following equation

$$\tau_R^{-1} = \frac{k_B T}{8\pi\eta R^3} \quad (6)$$

where $k_B T$ [J] is the thermal energy, η [Pa s] is the viscosity of water, and R [m] is the particles radius.[27] A value of ~50 s was estimated, which is lower than the time length our videos. In fact, to observe random trajectories the exposure time must be much larger than τ_R. **Figure 4** reports the comparison of the speed of microrobots at various conditions and the proposed interpretation based on electrochemical measurements. Different metal coatings led to different microrobots speeds. Figure 4(a) shows the average speed values calculated from the analysis of several microrobots (n > 10). Hematite/Pt microrobots display a higher speed (3.3 ± 0.4 μm s^{-1}) than hematite/Au ones (1.6 ± 0.8 μm s^{-1}). The presence of Pd in the bimetallic coatings results in an increase of the speed with respect to the single metal, since hematite/Au-Pd microrobots speed is 2.4 ± 0.3 μm s^{-1} while hematite/Pt-Pd microrobots speed is 4 ± 1 μm s^{-1}. This result is in agreement with the enhancement achieved in UV-light powered TiO_2 microrobots by consecutive sputtering of Ag and Au.[41] By adding low concentrations of H_2O_2 the speed of all microrobots obviously increases, however the trend between the different metal coatings is preserved. Hematite/Pt-Pd microrobots showed the highest speed of 8 ± 2 μm s^{-1} in 0.1 wt% H_2O_2, and 12 ± 4 μm s^{-1} in 1 wt% H_2O_2

(Supplementary Movie 3). It must be noted that a ten-fold increase of the fuel content does not produce a proportional increase of the speed, suggesting that hematite low electron mobility is the rate limiting step. Still, the speed of our hematite/Pt-Pd microrobots is comparable to or higher than other semiconductor-based Janus microrobots.[22-28]

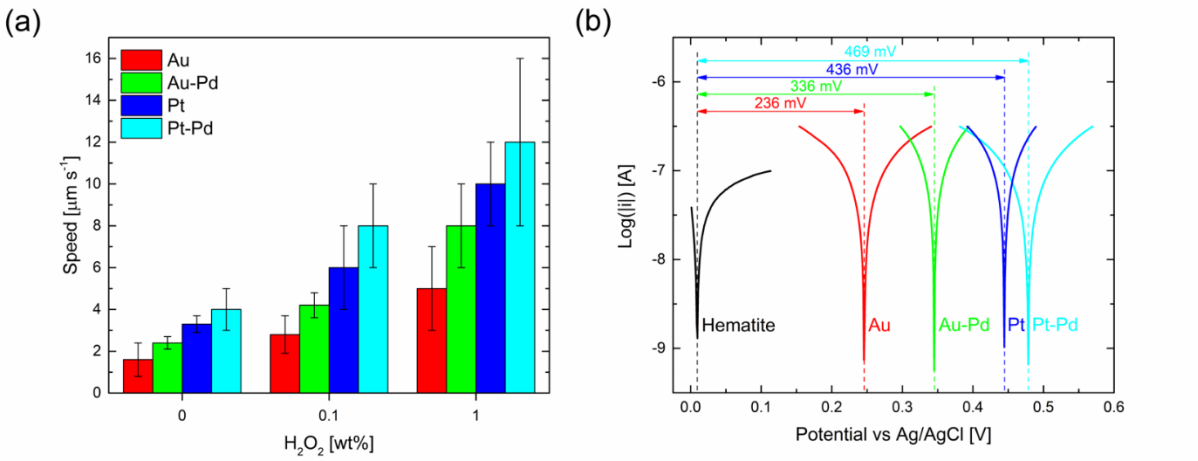

Figure 4. Comparison and understanding of the different speeds of light-powered hematite/metal Janus microrobots. (a) Speed at various concentrations of H_2O_2 under UV-light irradiation. (b) Tafel plots of hematite, Au, Au-Pd, Pt, Pt-Pd electrodes under UV-light irradiation in pure water.

To understand the reason for the differences in speed with diverse metal coatings, the mixed potential difference between the two faces of Janus microrobots, i.e. hematite and metal, were evaluated. In fact, it has been demonstrated that the larger is such potential difference, the higher is the speed.[24,28] Tafel experiments were conducted to measure the mixed potential of UV-light irradiated hematite, Au, Au-Pd, Pt and Pt-Pd electrodes, and Figure 4(b) reports the obtained results. The mixed potential difference follows the trend already observed for microrobots speed. Such a difference is almost doubled from Au (236 mV) to Pt (436 mV), in agreement with the two-fold increase in speed observed for hematite/Pt microrobots compared to hematite/Au. The bimetallic coatings result in larger potential differences with respect to the single metals (336 for Au-Pd, 469 for Pt-Pd), with Pt-Pd exhibiting the largest difference as well as speed. Therefore, we believe that speed

enhancement in bimetallic coating is attributed to the larger mixed potential difference. It must be noted that the work function of Pt is larger than hematite (Φ_{Pt} = 5.9 eV, $\Phi_{hematite}$ = 5.7 eV).[27,31] This leads to the upward bending of hematite energy bands, as illustrated in Figure 3, and to the formation of a relatively small Schottky barrier with 1.0 eV height, calculated as the difference between Φ_{Pt} and hematite electron affinity ($\chi_{hematite}$ = 4.9 eV).[31] On the contrary, Au work function (Φ_{Pt} = 5.2 eV) is lower than hematite, resulting in a downward bending of hematite energy bands and in the formation of an Ohmic contact.[43] On these bases, a higher charge separation and speed would be expected for hematite/Au Janus microrobots. However, our findings indicate that mixed potential difference and catalytic activity of the metal (Pt is more catalytic than Au for hydrogen evolution reaction) play the major role in determining the speed of semiconductor/metal Janus microrobots.[28]

The control over the on-off switching of motion with light and magnetic field navigability of hematite/metal Janus microrobots was examined (**Figure 5**). High concentrations of H_2O_2 and highly catalytic metal coatings (Pt, Pt-Pd) could lead to high speeds at the expense of a poor control over the light-induced on/off motion. In fact, even in absence of light irradiation, Pt and Pt-Pd catalyze H_2O_2 decomposition[42]

$$2H_2O_2 \xrightarrow{Pt,Pt-Pd} 2H_2O + O_2. \quad (7)$$

As a consequence, particles motion is obtained due to the resulting product gradient leading to self-diffusiophoresis, or due to the recoil energy of O_2 bubbles production (bubble-propelled motion). In our experiments we did not notice bubble-propulsion for the explored concentrations of H_2O_2. Hematite/Pt-Pd microrobots showed no clear self-diffusiophoretic motion in 0.1 wt% H_2O_2 without light irradiation. To corroborate this observation, several videos of hematite/Pt-Pd microrobots in 0.1 wt% H_2O_2 were tracked, and the mean square displacement (MSD) with and without UV-light irradiation were calculated. The magnitude of the MSD reflects the strength of the motion, while its functional dependence on time

characterizes the nature of the motion. The MSD [μm^2] after a fixed time interval Δt [s] can be defined as

$$\mathrm{MSD} = \langle (x(\Delta t) - x_0)^2 + (y(\Delta t) - y_0)^2 \rangle \quad (8)$$

where the brackets <> indicate an average over an ensemble of n particles (n > 20 microrobots in our case), x_0 and y_0 [μm] are the original coordinates of particles, and $x(\Delta t)$ and $y(\Delta t)$ [μm] are the coordinates of particles at the time Δt.[44] In the case of pure Brownian motion in a plane, the MSD of spherical particles obeys the relationship

$$\mathrm{MSD} = 4D\Delta t \quad (9)$$

where D [μm^2 s^{-1}] is the diffusion coefficient of microrobots. In contrast, a purely ballistic motion of particles results in the quadratic relationship of MSD with Δt

$$\mathrm{MSD} = 4D\Delta t + v^2\Delta t^2 \quad (10)$$

with v [μm s^{-1}] being particles speed.[27] When MSD ~ Δt^{α} with $\alpha > 1$ the transport is defined as "superdiffusive". As shown in Figure 5(a), the MSD of hematite/Pt-Pd microrobots without light irradiation (UV-off) increases linearly with time, proving that without light irradiation there is no self-diffusiophoresis or it is not sufficient to overcome the Brownian motion. Under light irradiation (UV-on), the MSD follows a parabola, in agreement with equation (10), indicating that the transport is superdiffusive due to the light-powered self-electrophoretic motion of microrobots. Based on equation (9) and (10), the diffusion coefficient of microrobots with and without light irradiation were calculated and reported in Figure 5(a). Upon light irradiation, a two-fold increase of D is observed, reaching 1.4 ± 0.1 μm^2 s^{-1} (inset in Figure 5(a)).

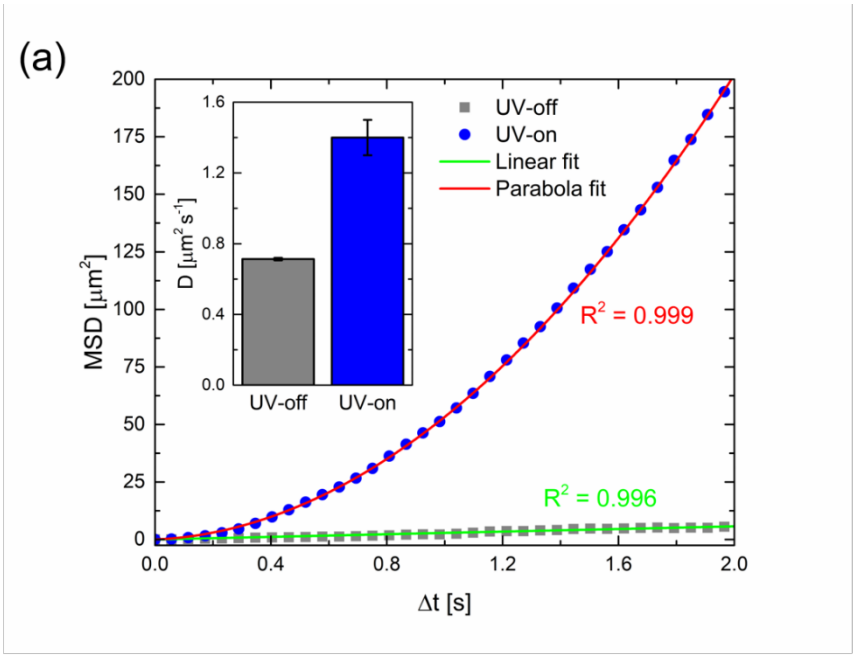
(a)
MSD [μm²]
Δt [s]
UV-off
UV-on
Linear fit
Parabola fit
R² = 0.999
R² = 0.996
D [μm² s⁻¹]
UV-off
UV-on

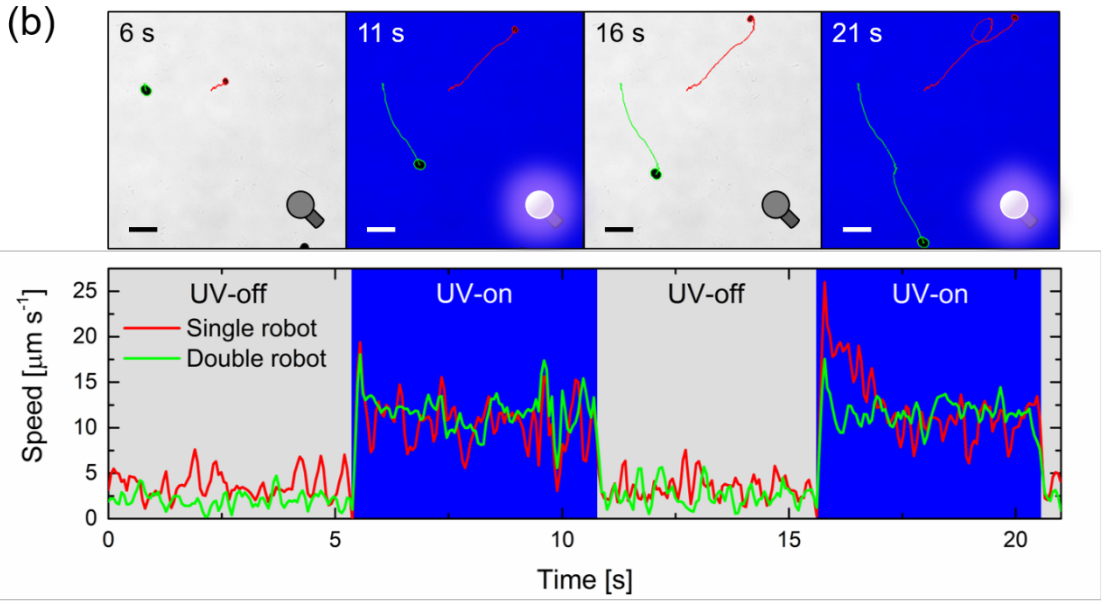
(b)
6 s
11 s
16 s
21 s
Speed [μm s⁻¹]
UV-off
Single robot
Double robot
UV-on
UV-off
UV-on
Time [s]

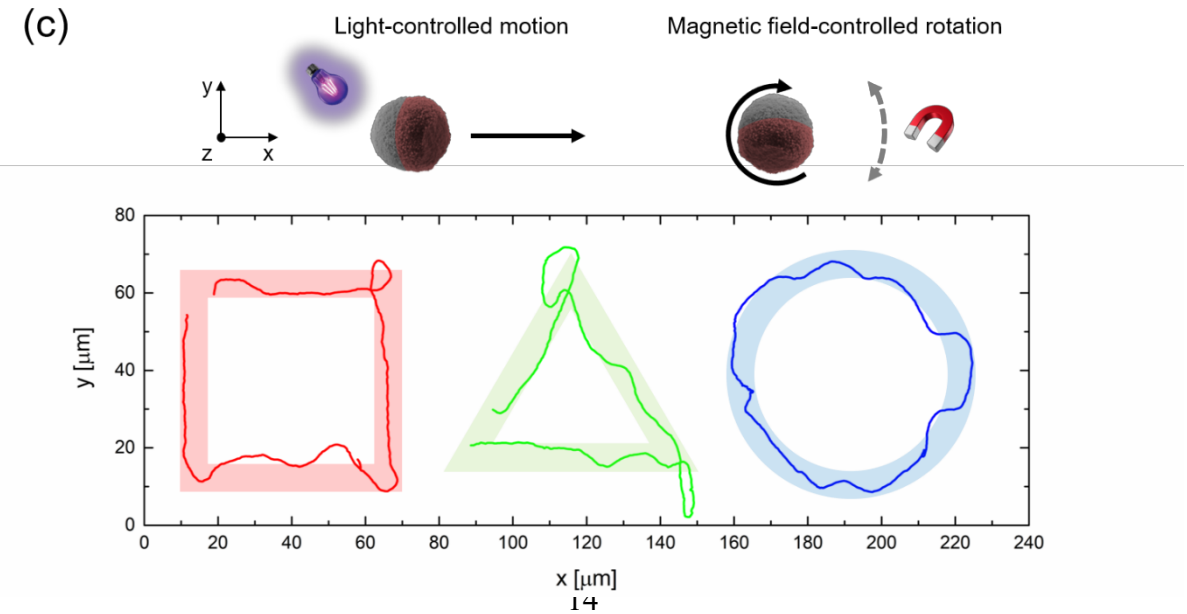
(c)
Light-controlled motion
Magnetic field-controlled rotation
y
z
x
y [μm]
x [μm]

Figure 5. Light/magnetic field-controlled motion of hematite/Pt-Pd microrobots. (a) MSD plots from tracking 20 microrobots with (UV-light on) and without (UV-light off) UV-light irradiation in 0.1 wt% H_2O_2 (the inset reports the diffusion coefficients obtained from fitting MSD plots with equations (9) and (10)). (b) Time-lapse tracking line images of single and double microrobots in 1 wt% H_2O_2 by on/off switching of UV-light irradiation at time intervals of ~5 s (scale bars are 20 μm). (c) Trajectories of a light-controlled magnetic field-navigated microrobot in 1 wt% H_2O_2 forming a square, a triangle and a circle.

In 1 wt% H_2O_2, a slow self-diffusiophoretic motion was observed for hematite/Pt-Pd microrobots in absence of light, but it did not affect their light-controlled on/off motion ability, as the self-electrophoresis under light irradiation was much more efficient. To demonstrate this feature, experiments with several UV-light on/off switching were performed. Figure 5(b) shows the time-lapse tracking line images of single and double hematite/Pt-Pd microrobots in 1 wt% H_2O_2 at time intervals of ~5 s (Supplementary Movie 4), and their corresponding speed. Both microrobots exhibit rapid light-controlled on/off motion capability in 1 wt% H_2O_2. Moreover, single and double microrobots have the same speed. This characteristic was observed also for the other metal coatings. Significant differences in speed were appreciated only for larger microrobots agglomerates (>3). In higher concentration of H_2O_2 (10 wt%), there is a higher speed under light irradiation (23 ± 5 μm s^{-1}) but no on/off switching of motion with light due to the higher efficiency of self-diffusiophoresis in dark (Supplementary Movie 5).

Generally, magnetic field navigation in Janus microrobots based on other photocatalytic semiconductors is achieved only by coating the semiconductor with a Ni layer before the deposition of the catalytic metal, as in the case of TiO_2/Ni/Au microrobots, or by incorporating/loading ferromagnetic nanoparticles.[45,46] Nevertheless, both approaches result in an increase of fabrication cost and complexity. Instead, the use of low-cost and abundant hematite as the photocatalytic semiconductor for the fabrication of light-powered Janus microrobots adds the advantage that they can be easily navigated using a magnetic field due to its weak ferromagnetic behavior. Even a small magnet is sufficient to induce the rotation of

hematite microspheres, and thus microrobots (Supplementary Movie 6). Given the light-controlled on/off motion feature of our Janus microrobots and the intrinsic magnetic field navigability of hematite, it is possible to control the trajectory of microrobots also at the high speeds obtained in 1 wt% H_2O_2, drawing squared, triangular and circular shapes as those reported in Figure 5(c) (Supplementary Movie 7).

2.3. Polyethylene glycol photodegradation

Micro/nanorobots have demonstrated the ability to remove and degrade a large variety of pollutants in water. Still, to the best of our knowledge, the degradation of polymer chains using such materials has never been shown. In this work, our hematite/metal Janus microrobots were employed for the capture and degradation of polyethylene glycol (PEG) with a high molecular weight of 4000, since PEG degradation can be easily evaluated by Matrix-Assisted Laser Desorption/Ionization Mass Spectrometry (MALDI-MS). Prior to photocatalytic experiments, the Zeta potential (ζ) of microrobots and PEG was measured at different pH (Figure S2), finding that at the optimal pH of 3, microrobots are positively charged (+64 mV) while PEG is negatively charged (-27 mV). Therefore, microrobots motion under light irradiation and electrostatic interactions with PEG dramatically enhance PEG capture. Simultaneously, photogenerated ROS induce the degradation of the captured PEG.

Hematite/Pt-Pd microrobots have been chosen for photocatalytic experiments because of their higher speed and superior photocatalytic activity. A control experiment in absence of microrobots was performed to clearly evaluate microrobots contribution. All samples were exposed to UV irradiation for 24 h in 1 wt% H_2O_2. **Figure 6** reports MALDI-MS spectra of PEG, UV-irradiated PEG, and microrobots-treated PEG. Signals corresponding to PEG macromolecular chains around 4000 mass decrease upon exposure to UV-light, producing oxidized polymer chains at lower masses. This result is in agreement with previous studies on

PEG photodegradation mechanism: H_2O_2 is decomposed under UV-light irradiation, forming OH· radicals which attack C-O bonds in PEG backbone.[47,48] Our UV lamp is not powerful enough to degrade completely PEG in 24 h. Instead, microrobots-treated PEG is almost totally degraded to short polymer chains with masses below 1000. A control experiment with bare hematite microspheres was conducted as well. Signals of high mass polymer chains (1500-3000) are detected (Figure S3), proving the superior PEG degradation ability of microrobots due to their self-propulsion and improved charge separation at the hematite/Pt-Pd junction.

Microrobots-induced PEG degradation involves photocatalysis, Fenton and photo-Fenton reaction. To identify the dominant process, additional experiments were conducted in absence of H_2O_2 or UV-light, evidencing the specific contribution of photocatalysis or Fenton reaction, respectively. The obtained MALDI-MS spectra indicate that sole photocatalysis or Fenton reaction leads to a poor PEG degradation (Figure S4). Thus, photo-Fenton reaction represents the main degradation mechanism. This conclusion is consistent with previous studies on ethylene glycol degradation through photo-Fenton reaction, where it was demonstrated that, in presence of UV-light irradiation and H_2O_2, Fe^{3+} ions increase the production of OH· radicals, favoring the complete mineralization of ethylene glycol.[49] To demonstrate this, we carried out an experiment using EDTA as photogenerated holes scavenger, finding that PEG degradation is almost completely hindered (Figure S5).[50] This confirms the fundamental role of photogenerated holes in producing more OH· radicals for PEG degradation.

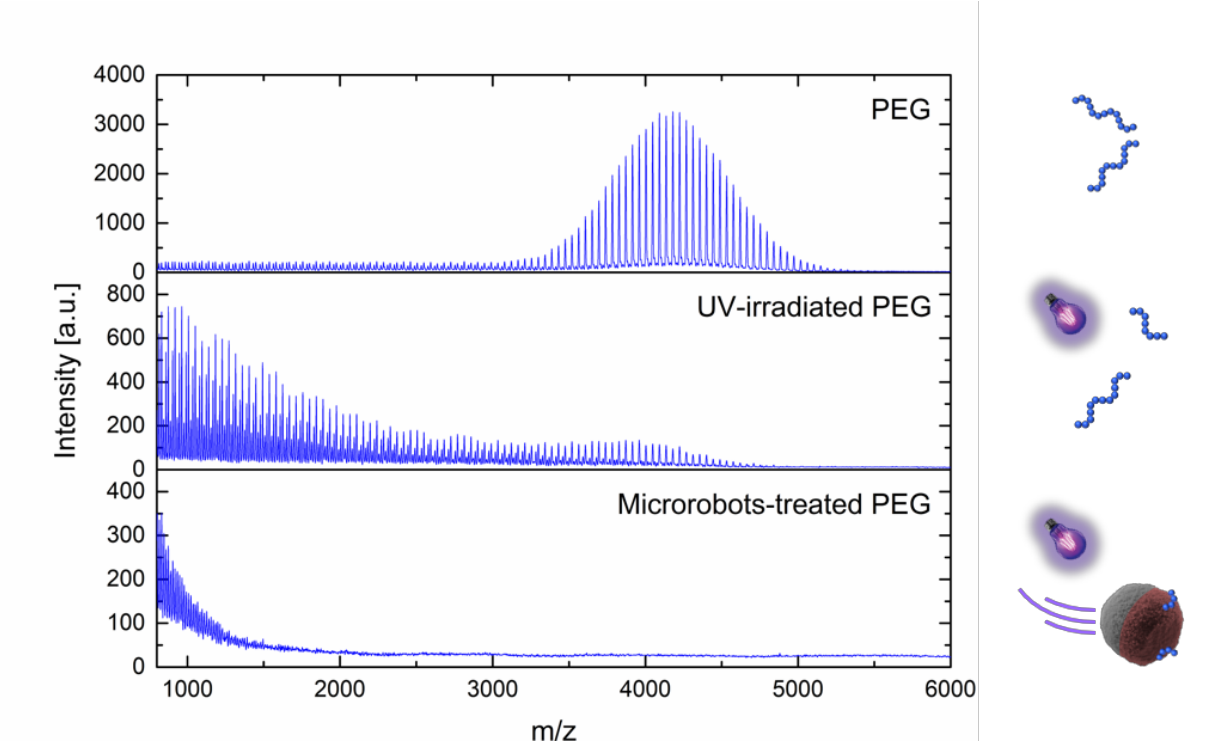

Figure 6. PEG photodegradation. From top to bottom, MALDI-MS spectra of untreated PEG, PEG treated for 24 h under UV-light irradiation in 1 wt% H_2O_2, and PEG treated for 24 h with hematite/Pt-Pd Janus microrobots under UV-light irradiation in 1 wt% H_2O_2.

The effect of microrobots concentration and treatment duration was also examined. It was noted that a concentration of microrobots as low as 0.5 mg ml^{-1} is sufficient to achieve the effective degradation of PEG, as the MALDI-MS spectra recorded for 0.5, 1 and 2 mg ml^{-1} microrobots are similar (Figure S5). Regarding treatment duration, PEG degradation was not completed after 8 or 16 h. Nonetheless, the process can be accelerated by increasing the power of the UV-light source.

To corroborate MALDI-MS results, the size distribution of bare PEG and microrobots-treated PEG was evaluated by dynamic light scattering (DLS) experiments (Figure S8). Based on PEG monomer length (0.35 nm) and number of subunits in PEG 4000 (~90), an average linear length of ~30 nm is expected for PEG.[51] In the untreated PEG, multiple sizes ranging from few tens of nm to few µm were observed, with the latter having higher intensity. This suggests that aggregations of polymer chains occur in water. However, in the microrobots-treated PEG, a higher peak intensity at the small size of 1 nm is found. Such datum further

verifies the degradation of PEG into low mass products, in agreement with MALDI-MS analysis.

The excellent PEG degradation ability of our microrobots is attributed to their self-propulsion enhancing electrostatic PEG capture, to the rational engineering of the hematite/metal interface leading to an improved charge separation and photocatalytic efficiency, and to the catalyzed photo-Fenton reaction. Since they were capable of breaking the strong chemical bonds in polymer chains, we expect high performances against other contaminants, among which microplastics, persistent organic pollutants (POPs) and pathogenic bacteria. It is worth noting that when dealing with plastic materials, secondary pollution resulting from toxic photodegradation products (e.g. aromatic ketones, phthalates and their derivatives) must be considered for practical applications. Magnetic field navigability of our microrobots allows to collect and, potentially reuse them in new treatments. Furthermore, they can be produced on large scale, and employed for the degradation of pollutants in larger volumes of water in confined systems. The utilization of 1 wt% H_2O_2 is generally considered a limitation for environmental applications. Still, using commercial hydrogen peroxide test strips, we demonstrated that the concentrations of H_2O_2 in the processed water decreased from 10000 ppm to less than 2 ppm after 24 h long treatment with microrobots (Figure S9). This value is lower than the allowed limit of H_2O_2 in drinking water 8 ppm stated by the regulation No 528/2012 of the European Union. Hence, H_2O_2 does not constitute a limit of the proposed remediation approach.

3. Conclusion

We reported the fabrication of hematite/metal Janus microrobots that move under light irradiation and in absence of fuel. Hematite microspheres were synthesized by a low-cost and large-scale hydrothermal method and covered with different metals to obtain Janus

microrobots. This design improved the electron transfer from hematite to the metal, suppressing the characteristic fast electron-hole recombination rate in hematite. Mean square displacement (MSD) calculations proved that microrobots undergo pure Brownian motion in dark, and self-electrophoretic motion under light-irradiation. They also showed rapid on/off capability with light irradiation, and the possibility to control the direction of the motion by using a magnetic field. In this way, a precise control over their trajectories was attained, holding great potential for their future application in cargo transport. The various metal coatings (Au, Au-Pd, Pt, and Pt-Pd) led to different speeds. In particular, the bimetallic coating resulted in higher speed compared to the single metal. While this behavior in previous works has been attributed to the synergistic effect of the two metals, we observed a larger mixed potential difference for the bimetallic coating by Tafel measurements as the reason for the enhanced self-electrophoresis. We demonstrated the degradation of polymers in water using self-propelled microrobots. The degradation ability of microrobots was evaluated towards high molecular weight polyethylene glycol (PEG), which represents the ideal polymer to be analyzed by Matrix-Assisted Laser Desorption/Ionization Mass Spectrometry (MALDI-MS). Microrobots proved the ability to completely degrade PEG chains into low mass products. Their active motion, pH-programmable electrostatic PEG capture, improved charge separation due to the hematite/metal interface, and catalyzed photo-Fenton reaction are responsible for this result. This work presents a new approach for the photodegradation of polymeric and plastic materials, as well as other pollutants, in water.

4. Experimental Section

Fabrication of Hematite/Metal Janus Microrobots: Hematite (α-Fe_2O_3) microspheres were synthesized by a simple hydrothermal reaction. An aqueous solution of 1 M $FeCl_3$ (Sigma-Aldrich, 97%) was prepared using ultra-pure water (18 MΩ cm) and transferred into a 50 ml

Teflon-lined stainless-steel autoclave. The autoclave was heated at 160°C for 20 h, and then cooled down to room temperature naturally. Afterwards, the obtained reddish-brown particulate was collected by centrifugation (3000 rpm for 3 min), washed two times with ultra-pure water and absolute ethanol, respectively, and dried in air at 60°C for 6 h. To fabricate Janus microrobots, an aqueous suspension of hematite microspheres (5 mg ml^{-1}) was dropped on glass slides and dried overnight. Different metals (Au, Au-Pd 80:20, Pt, Pt-Pd 80:20, from Neyco) were asymmetrically deposited on hematite microspheres by sputtering method. The thickness of the deposited metal (30 nm) was controlled by a quartz crystal microbalance. The resulting hematite/metal Janus microrobots were detached from glass slides using a scalpel.

Characterization of Hematite/Metal Janus Microrobots: A Tescan MIRA 3 XMU scanning electron microscope (SEM) equipped with an energy-dispersive X-ray detector (EDX, Oxford Instruments) was used to characterize samples morphology and perform elemental mapping. The crystalline structure of hematite microspheres was determined in Bragg-Brentano geometry using a Rigaku SmartLab 9kW diffractometer, equipped with a high-brightness Cu K_α rotating anode X-ray tube operating at 45 kV and 200 mA. The chemical composition of hematite microspheres was examined by X-ray photoelectron spectroscopy (XPS) Kratos Analytical Axis Supra, using monochromatic Al K_α (1486.7 eV) excitation source. All peaks were calibrated to the adventitious C 1s peak at 284.8 eV. XPS spectra were fitted using CasaXPS software. A Malvern Panalytical Zetasizer Ultra instrument was used for zeta potential and size distribution measurements at pH 7 and 3 in ultra-pure water.

Motion Behaviour of Hematite/Metal Janus Microrobots: The light-powered motion of microrobots was observed and recorded using a Nikon ECLIPSE Ti2 inverted optical microscope equipped with a Hamamatsu digital camera C13440-20CU. In a typical

experiment, an aqueous suspension of microrobots was dispersed in ultra-pure water and dropped on a glass slide, eventually adding H_2O_2 (Merck, 30 wt%) at concentrations of 0.1, 1 and 10 wt%. No surfactant was employed in these experiments. A 365 nm UV LED (CoolLED pE-100) was used to induce microrobots motion at 500 mW cm^{-2} intensity. NIS Elements Advanced Research software was used to both record and analyse videos of microrobots. Speed values and mean square displacement (MSD) calculations result from the average of more than 10 different microrobots, each of them examined for several on/off switching of UV-light irradiation. A commercial magnet (15x15x8 mm, N38, SilneMagnety) was used for magnet navigation experiments.

Electrochemical Measurements: Tafel experiments were performed in a customized photoelectrochemical setup with a 365 nm UV LED (700 mA powered LZ4-04UV00, LedEngin Inc.) in a two-electrode configuration connected to a Metrohm AUTOLAB potentiostat. The hematite working electrode was prepared by dropping 100 µl of a 5 mg ml^{-1} aqueous suspension of hematite microspheres on a commercial ITO-covered glass slide (1x2 cm^2, Sigma-Aldrich, 8-12 Ω sq^{-1}), followed by overnight drying. Metal working electrodes were obtained by sputtering metals (100 nm) on ITO-covered glass slides. An Ag/AgCl (1 M KCl internal solution) commercial electrode was used as both counter and reference electrode since only a small amount of current was passed. Ultra-pure water served as electrolyte to mimicry fuel-free motion experiments. Tafel plot measurements were recorded at a scan rate of 5 mV s^{-1} from 0 to 0.6 V vs Ag/AgCl with and without UV-light irradiation on the working electrodes (1x1 cm^2 immersed area).

Polyethylene Glycol Photodegradation: The photodegradation ability of microrobots was evaluated towards polyethylene glycol (PEG, Mw 4000, Alfa Aesar) under UV-light irradiation. 1 mg of PEG 4000 and different amounts of microrobots (0.5, 1 and 2 mg ml^{-1})

were added to 1 ml of ultra-pure water solution (pH 3) with 1 wt% H_2O_2 in disposable cuvettes. Similarly, three control samples were prepared: i) without addition of microrobots; ii) with 1 mg ml^{-1} bare hematite microspheres; iii) with 20 mg ml^{-1} ethylenediaminetetraacetic acid (EDTA, Sigma-Aldrich, 99.4-100.6%) as photogenerated holes scavenger. Cuvettes were irradiated for different durations (8, 16 and 24 h) using a 365 nm UV LED lamp (9 W) as the light source. After photodegradation experiments, each solution was centrifugated (3500 rpm for 5 min), and the supernatant solution was collected and stored for further analyses. PEG 4000 degradation was evaluated by UltrafleXtreme Matrix-Assisted Laser Desorption/Ionization Mass Spectrometry (MALDI-MS, Bruker Daltonics, Bremen, Germany) operated in linear positive detection mode. A three-layer sample preparation technique was used: a layer of 50 mg ml^{-1} trans-2-[3-(4-tert-butylphenyl)-2-2-methyl-2-propenylidene]malononitrile in acetone (0.2 µl) was dried on a stainless steel target, and then overlaid with a saturated solution of NaI in acetone (0.2 µl) and with the sample solution (0.2 µl). The content of H_2O_2 in water before and after the treatment was measured through commercial hydrogen peroxide test strips (SimplexHealth).

Supporting Information

Supporting Information is available from the Wiley Online Library or from the author.

Acknowledgements

M.P. was supported by Ministry of Education, Youth and Sports (Czech Republic) grant LL2002 under ERC CZ program. CzechNanoLab project LM2018110 funded by MEYS CR is gratefully acknowledged for the financial support of the measurements/sample fabrication at CEITEC Nano Research Infrastructure. CIISB, Instruct-CZ Centre of Instruct-ERIC EU

consortium, funded by MEYS CR infrastructure project LM2018127, is gratefully acknowledged for the financial support of the measurements at the CEITEC Proteomics Core Facility.

Author Contributions

M.Ur. designed the experiments, performed the fabrication and characterization of microrobots and electrochemical measurements. M.Us. conducted PEG photodegradation experiments. M.Ur. and M.P. conceived the idea. M.P. supervised the research. All authors gave approval to the final version of the manuscript.

Received: ((will be filled in by the editorial staff))

Revised: ((will be filled in by the editorial staff))

Published online: ((will be filled in by the editorial staff))

References

[1] A. Chamas, H. Moon, J. Zheng, Y. Qiu, T. Tabassum, J. H. Jang, M. Abu-Omar, S. L. Scott, S. Suh, *ACS Sustain. Chem. Eng.* **2020**, *8*, 3494–3511.

[2] R. Siddique, J. Khatib, I. Kaur, *Waste Manage.* **2008**, *28*, 1835–1852.

[3] O. Tsydenova, M. Bengtsson, *Waste Manage.* **2011**, *31*, 45–58.

[4] J. R. Jambeck, R. Geyer, C. Wilcox, T. R. Siegler, M. Perryman, A. Andrady, R. Narayan, K. L. Law, *Science* **2015**, *347*, 768–771.

[5] J. Gigault, A. ter Halle, M. Baudrimont, P. Y. Pascal, F. Gauffre, T. H. Phi, H. El Hadri, B. Grassl, S. Reynaud, *Environ. Pollut.* **2018**, *235*, 1030–1034.

[6] A. L. Andrady, *Mar. Pollut. Bull.* **2011**, *62*, 1596–1605.

[7] R. C. Thompson, Y. Olsen, R. P. Mitchell, A. Davis, S. J. Rowland, A. W. G. John, D. McGonigle, A. E. Russell, *Science* **2004**, *304*, 838.

[8] A. Cózar, F. Echevarríaa, J. I. González-Gordilloa, X. Irigoienb, B. Úbedaa, S. Hernández-Leónd, A. T. Palmae, S. Navarrof, J. García-de-Lomasa, A. Ruizg, M. L. Fernández-de-Puellesh, C. M. Duartei, *Proc. Natl. Acad. Sci.* **2014**, *111*, 10239–10244.

[9] R. Geyer, J. R. Jambeck, K. L. Law, *Sci. Adv.* **2017**, *3*, e1700782.

[10] J. Shang, M. Chai, Y. Zhu, *J. Solid State Chem.* **2003**, *174*, 104–110.

[11] M. N. Chong, B. Jin, C. W. Chow, C. Saint, *Water Res.* **2010**, *44*, 2997–3027.

[12] K. Villa, L. Děkanovský, J. Plutnar, J. Kosina, M. Pumera, *Adv. Funct. Mater.* **2020**, *30*, 2007073.

[13] M. Safdar, J. Simmchen, J. Jänis, *Environ, Sci. Nano* **2017**, *4*, 1602–1616.

[14] W. Gao, J. Wang, *ACS Nano* **2014**, *8*, 3170–3180.

[15] J. Parmar, D. Vilela, K. Villa, J. Wang, S. Sánchez, *J. Am. Chem. Soc.* **2018**, *140*, 9317–9331.

[16] Y. Ying, M. Pumera, *Chem. Eur. J.* **2019**, *25*, 106–121.

[17] F. Novotný, H. Wang, M. Pumera, *Chem* **2020**, *6*, 867–884.

[18] H. Wang, M. Pumera, *Chem. Soc. Rev.* **2020**, *49*, 3211–3230.

[19] J. Li, V. V. Singh, S. Sattayasamitsathit, J. Orozco, K. Kaufmann, R. Dong, W. Gao, B. Jurado-Sanchez, Y. Fedorak, J. Wang, *ACS Nano* **2014**, *8*, 11118–11125.

[20] M. Fernández-Medina, M. A. Ramos-Docampo, O. Hovorka, V. Salgueiriño, B. Städler, *Adv. Funct. Mater.* **2020**, *30*, 1908283.

[21] K. Villa, F. Novotný, J. Zelenka, M. P. Browne, T. Ruml, M. Pumera, *ACS Nano* **2019**, *13*, 8135–8145.

[22] L. Kong, C. C. Mayorga-Martinez, J. Guan, M. Pumera, *Small* **2019**, *16*, 1903179.

[23] D. Zhou, Y. C. Li, P. Xu, N. S. McCool, L. Li, W. Wang, T. E. Mallouk, *Nanoscale* **2017**, *9*, 75–78.

[24] R. Dong, Y. Hu, Y. Wu, W. Gao, B. Ren, Q. Wang, Y. Cai, *J. Am. Chem. Soc.* **2017**, *139*, 1722–1725.

[25] L. Kong, C. C. Mayorga-Martinez, J. Guan, M. Pumera, *ACS Appl. Mater. Interfaces* **2018**, *10*, 22427–22434.

[26] A. M. Pourrahimi, K. Villa, Y. Ying, Z. Sofer, M. Pumera, *ACS Appl. Mater. Interfaces* **2018**, *10*(49), 42688-42697.

[27] A. M. Pourrahimi, K. Villa, C. L. Manzanares Palenzuela, Y. Ying, Z. Sofer, M. Pumera, *Adv. Funct. Mater.* **2019**, *29*, 1808678.

[28] T. Maric, M. Z. M. Nasir, R. D. Webster, M. Pumera, *Adv. Funct. Mater.* **2020**, *30*, 1908614.

[29] L. Wang, A. Kaeppler, D. Fischer, J. Simmchen, *ACS Appl. Mater. Interfaces* **2019**, *11*, 32937–32944.

[30] P. Liao, M. C. Toroker, E. A. Carter, *Nano Lett.* **2011**, *11*, 1775–1781.

[31] C. Lohaus, A. Klein, W. Jaegermann, *Nat. Commun.* **2018**, *9*, 1–7.

[32] S. Lee, J. W. Park, *Sustainability* **2020**, *12*, 2866.

[33] J. Palacci, S. Sacanna, A. P. Steinberg, D. J. Pine, P. M. Chaikin, *Science* **2013**, *339*, 936–940.

[34] J. Palacci, S. Sacanna, A. Vatchinsky, P. M. Chaikin, D. J. Pine, *J. Am. Chem. Soc.* **2013**, *135*, 15978–15981.

[35] J. Palacci, S. Sacanna, A. Abramian, J. Barral, K. Hanson, A. Y. Grosberg, D. J. Pine, P. M. Chaikin, *Sci. Adv.* **2015**, *1*, e1400214.

[36] Z. Lin, T. Si, Z. Wu, C. Gao, X. Lin, Q. He, *Angew. Chem.* **2017**, *129*, 13702–13705.

[37] Z. Lin, X. Fan, M. Sun, C. Gao, Q. He, H. Xie, *ACS Nano* **2018**, *12*, 2539–2545.

[38] C. Fruijtier-Pölloth, *Toxicology* **2005**, *214*, 1–38.

[39] G. S. Parkinson, *Surf. Sci. Rep.* **2016**, *71*, 272–365.

[40] G. F. Moreira, E. R. Peçanha, M. B. Monte, L. S. Leal Filho, F. Stavale, *Miner. Eng.* **2017**, *110*, 96–103.

[41] Z. Xiao, J. Chen, S. Duan, X. Lv, J. Wang, X. Ma, J. Tang, W. Wang, *Chem. Commun.* **2020**, *56*, 4728–4731.

[42] Y. Ying, A. M. Pourrahimi, C. L. Manzanares-Palenzuela, F. Novotny, Z. Sofer, M. Pumera, *Small* **2019**, 1902944.

[43] Y. Ishida, J. K. Jung1, M. S. Kim, J. Kwon, Y. S. Kim, D. Chung, I. Song, C. Kim, T. Otsu, Y. Kobayashi, *Commun. Phys.* **2020**, *3*, 1–8.

[44] J. Orozco, B. Jurado-Sanchez, G. Wagner, W. Gao, R. Vazquez-Duhalt, S. Sattayasamitsathit, M. Galarnyk, A. Cortes, D. Saintillan, J. Wang, *Langmuir* **2014**, *30*, 5082–5087.

[45] R. Dong, Q. Zhang, W. Gao, A. Pei, B. Ren, *ACS Nano* **2016**, *10*, 839–844.

[46] K. Yuan, V. de la Asunción-Nadal, B. Jurado-Sánchez, A. Escarpa, *Chem. Mater.* **2020**, *32*, 1983–1992.

[47] J. A. Giroto, A. C. Teixeira, C. A. Nascimento, R. Guardani, *Ind. Eng. Chem. Res.* **2010**, *49*, 3200–3206.

[48] S. P. Vijayalakshmi, G. Madras, *J. Appl. Polym. Sci.* **2006**, *100*, 3997–4003.

[49] B. D. McGinnis, V. D. Adams, E. J. Middlebrooks, *Water Res.* **2000**, *34*, 2346–2354.

[50] Q. Lu, Y. Zhang, S. Liu, *J. Mater. Chem. A* **2015**, *3*, 8552–8558.

[51] C. Cruje, D. B. Chithrani, *J. Nanomed. Res* **2014**, *1*, 00006.

Novel hematite-based Janus microrobots are presented, showing self-propulsion in pure water under light irradiation and magnetic field-controlled navigation. Owing to their active motion and catalyzed photo-Fenton reaction, microrobots are able to catch and consequently degrade high molecular weight polyethylene glycol in water. This result extends the potential application scope of microrobots to the degradation of polymer and plastic waste, a pressing environmental problem.

M. Urso, M. Ussia, M. Pumera*

Breaking polymer chains with self-propelled light-controlled navigable hematite microrobots

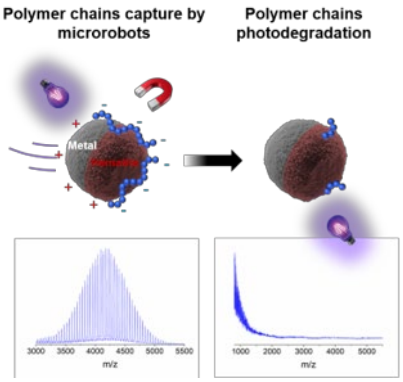

Supporting Information

Breaking polymer chains with self-propelled light-controlled navigable hematite microrobots

*Mario Urso, Martina Ussia, and Martin Pumera**

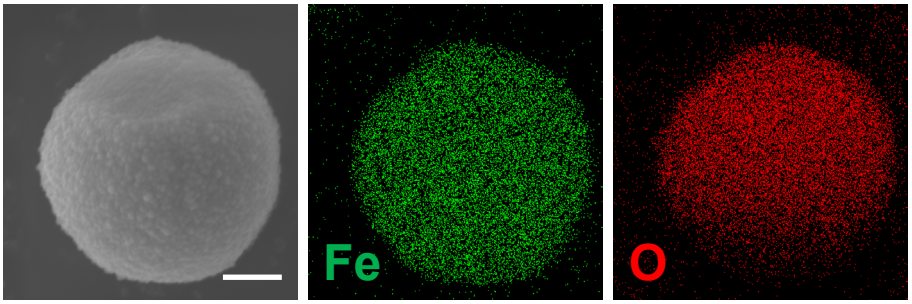

Figure S1. EDX elemental mapping images of a hematite microsphere (scale bar is 1 μm).

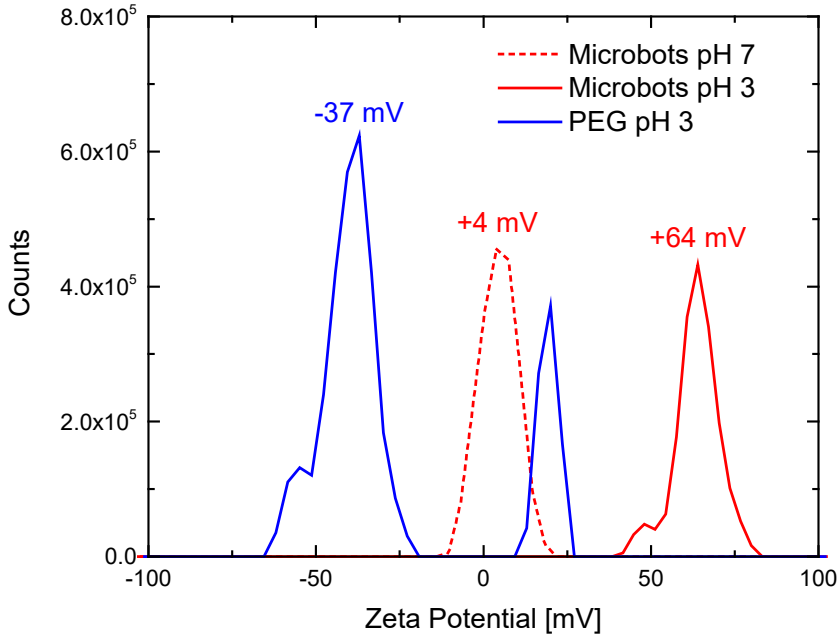

Figure S2. Zeta potential of hematite/Pt-Pd Janus microrobots and PEG in pure water at different pH measured by DLS.

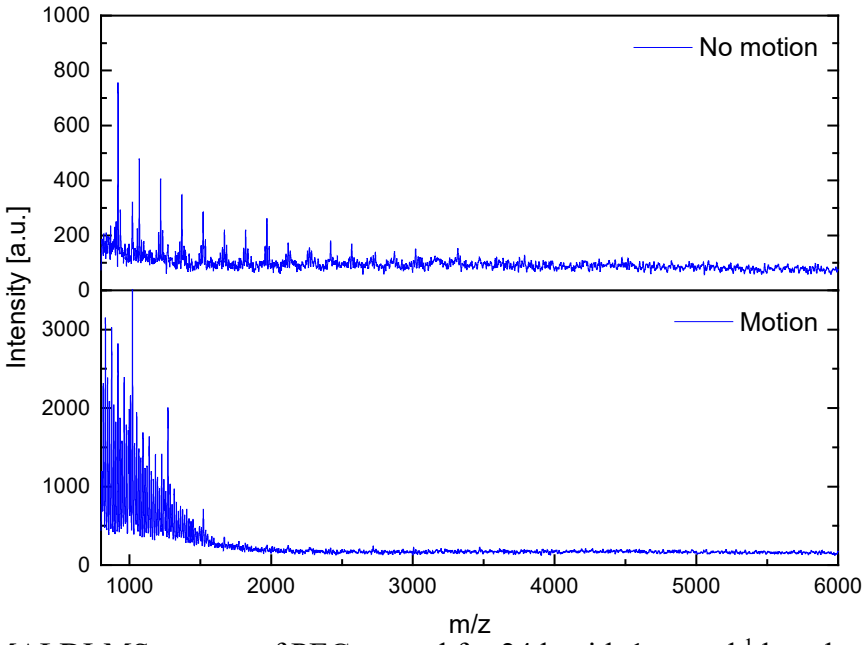

Figure S3. MALDI-MS spectra of PEG treated for 24 h with 1 mg ml^{-1} bare hematite microspheres (no motion) and 1 mg ml^{-1} hematite/Pt-Pd Janus microrobots (motion) under UV-light irradiation in 1 wt% H_2O_2.

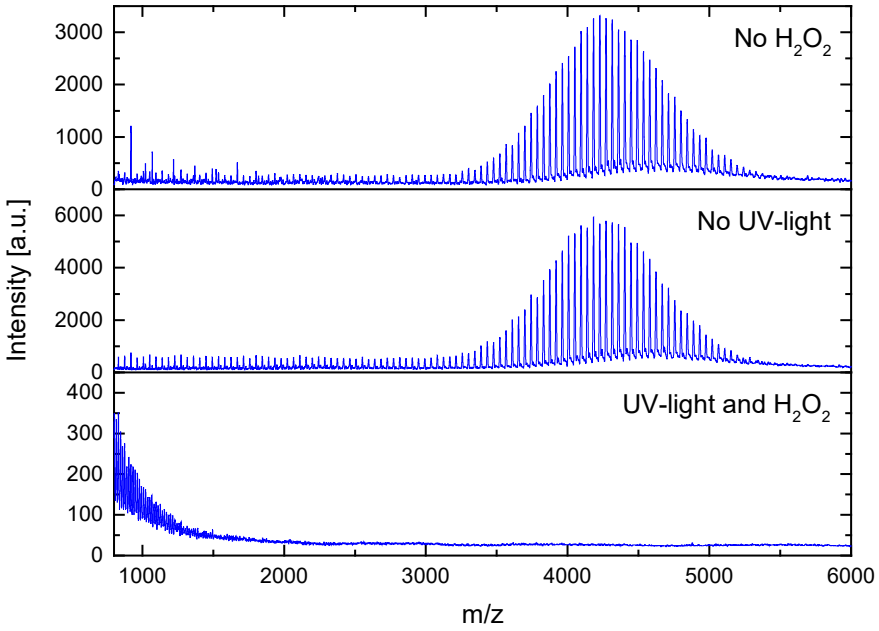

Figure S4. From top to bottom, MALDI-MS spectra of PEG treated for 24 h with 2 mg ml^{-1} hematite/Pt-Pd Janus microrobots under UV-light irradiation and no H_2O_2, in 1 wt% H_2O_2 and no UV-light, UV-light irradiation in 1 wt% H_2O_2.

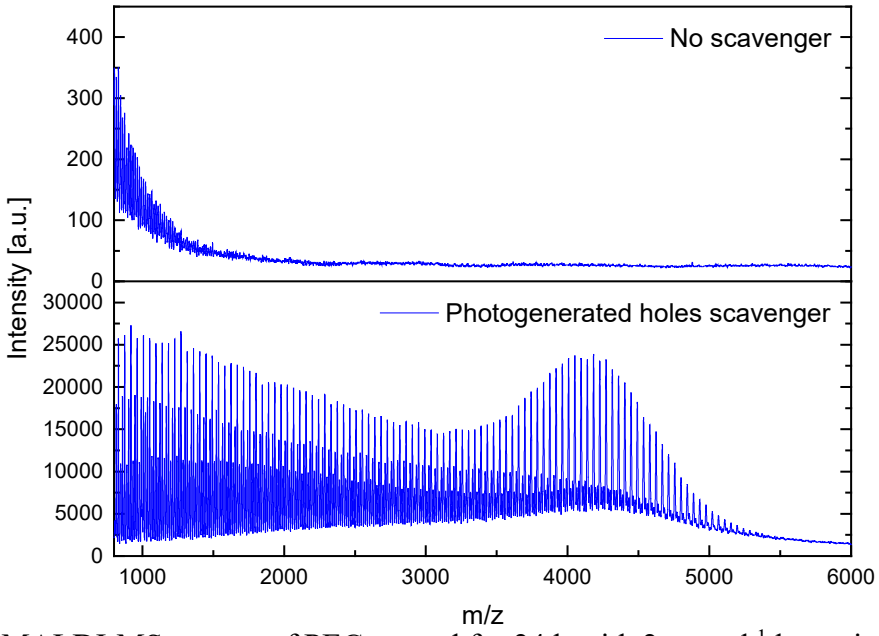

Figure S5. MALDI-MS spectra of PEG treated for 24 h with 2 mg ml^{-1} hematite/Pt-Pd Janus microrobots under UV-light irradiation in 1 wt% H_2O_2 in absence (no scavenger) and in presence (photogenerated holes scavenger) of 20 mg ml^{-1} EDTA.

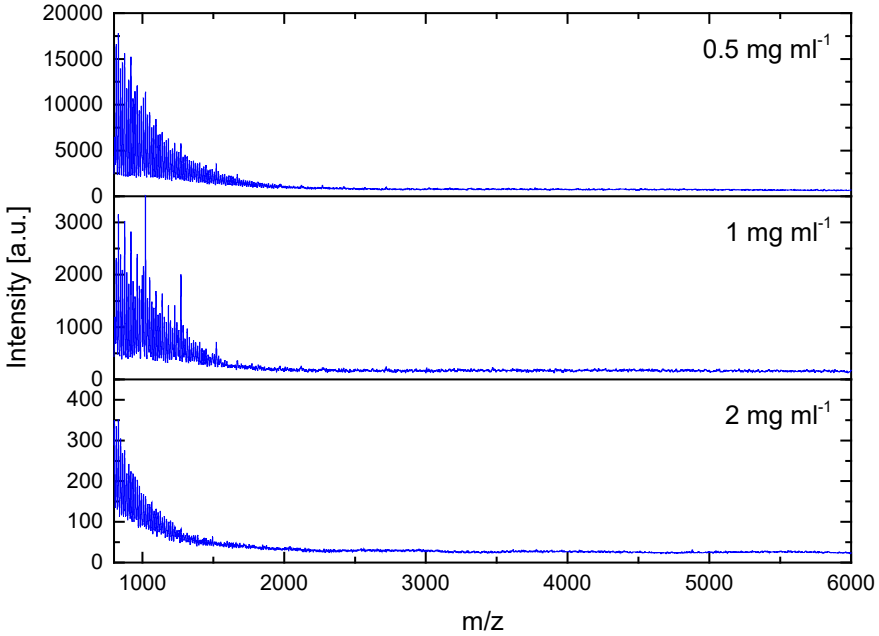

Figure S6. From top to bottom, MALDI-MS spectra of PEG treated for 24 h with 0.5, 1 and 2 mg ml^{-1} hematite/Pt-Pd Janus microrobots under UV-light irradiation in 1 wt% H_2O_2.

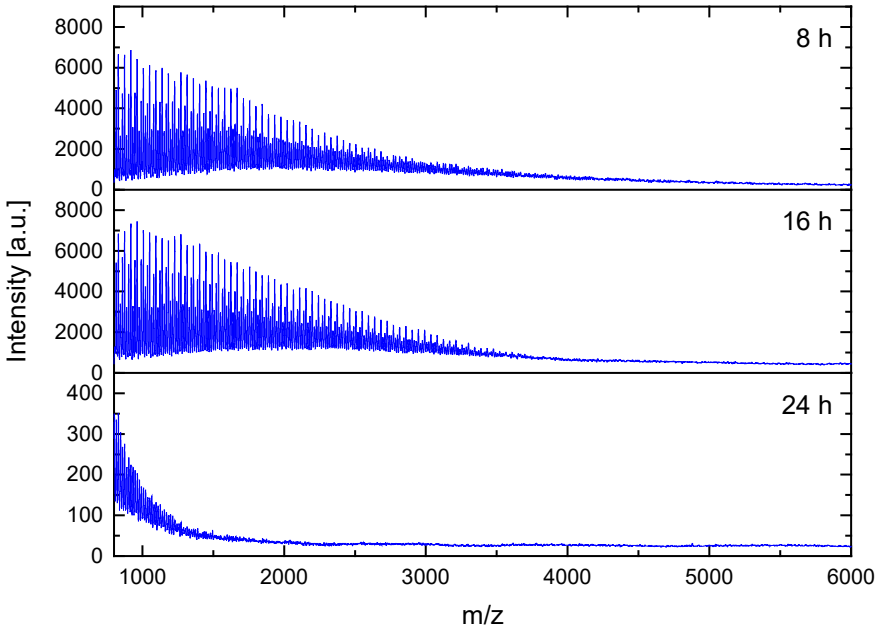

Figure S7. From top to bottom, MALDI-MS spectra of PEG treated for 8, 16 and 24 h with 2 mg ml^{-1} hematite/Pt-Pd Janus microrobots under UV-light irradiation in 1 wt% H_2O_2.

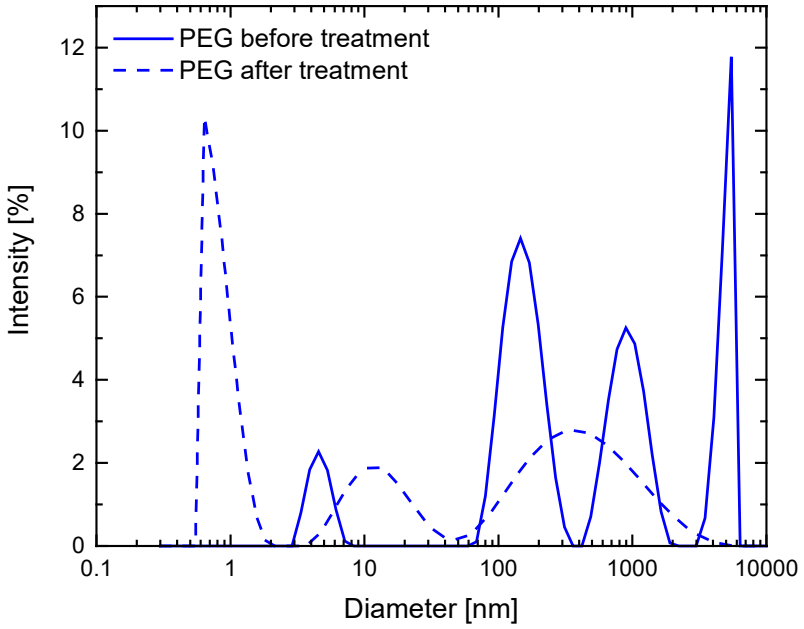

Figure S8. Size distribution of PEG before and after the treatment for 24 h with 2 mg ml^{-1} hematite/Pt-Pd microrobots under UV-light irradiation in 1 wt% H_2O_2.

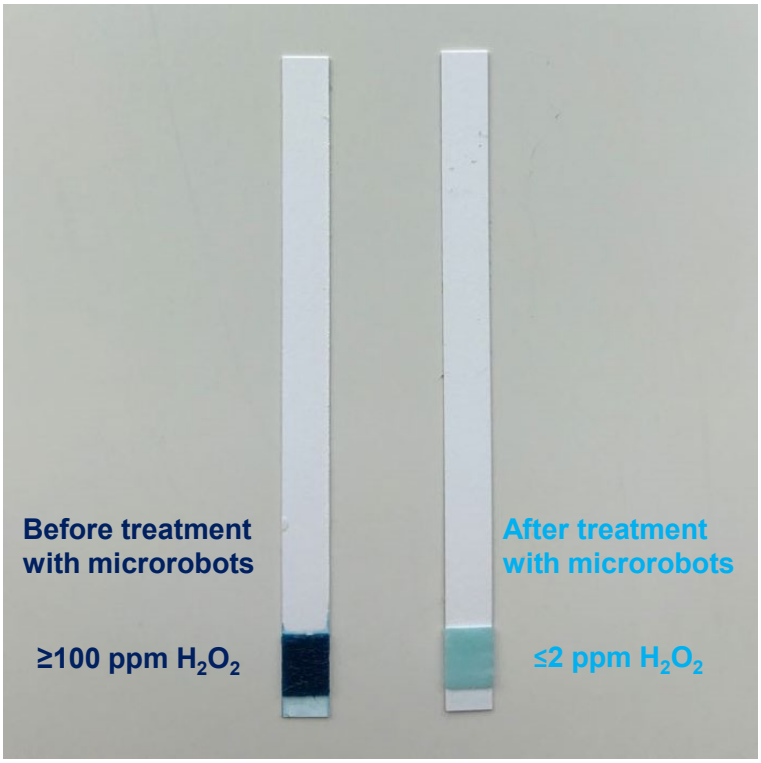

Figure S9. Photo of commercial hydrogen peroxide test strips immersed in the water solution for PEG photodegradation before (left) and after (right) the treatment for 24 h with 2 mg ml^{-1} hematite/Pt-Pd microrobots under UV-light irradiation in 1 wt% H_2O_2.